An Adaptive High-Order Finite-Volume Algorithm for Electromagnetic Fields

Scott Polak * and Xinfeng Gao†

Computational Fluid Dynamics and Propulsion Laboratory

Colorado State University, Fort Collins, CO 80523, USA

This work extends the development of a multi-fluid model for plasmas in the continuum regime by addressing a solution methodology to the electromagnetic equations. The multi-fluid model is based on a fourth-order, finite volume method algorithm which utilizes adaptive mesh refinement. The fluid equations and electromagnetic equations are coupled through their source terms. For the current work, we consider traditional source terms in Maxwell's equations; that is, where source terms are related to the density and flux of a single species only, electrons. To handle the mathematical over-constraint imposed by divergence terms in the electromagnetic equations, we utilize the approach of introducing divergence correction potentials to form a hyperbolic-only arrangement of the governing equations. For the electromagnetic flux calculation, a Harten–Lax–van Leer contact wave approach is used to solve the Riemann problem and resolve the discontinuity on faces. Verification of the algorithm accuracy is provided by analyzing L_p-norms of the error for the conservative solution variables, and validation is provided by comparing numerical model results to analytical solutions of simplified electromagnetic wave problems. Finally, we conclude with a discussion of the current results and a road map for future development work on the multi-fluid plasma model.

I. Nomenclature

$\vec{\nabla}$	gradient operator, default
$\vec{\nabla}\cdot$	divergence operator
$\vec{\nabla}\times$	curl operator
$\vec{E}$	electric field
$\vec{B}$	magnetic field
$\vec{j}$	electric current density
ρ	electric charge density
ϵ_0	permittivity of free space
μ_0	permeability of free space
c	speed of light
$\mathbf{U}$	vector of solution variables
$\vec{\mathbf{F}}$	tensor of hyperbolic flux terms
$\mathbf{S}$	vector of source terms
Φ	error correction potential
Ψ	error correction potential
χ	error correction wave speed
λ	error correction wave speed
$\vec{n}$	outward face-normal unit vector

II. Introduction

Previously, we have laid the groundwork for a multi-fluid approach to modeling non-equilibrium, continuum-regime plasmas.[1] The algorithm is based on a fourth-order, finite-volume-method (FVM) with adaptive mesh refinement (AMR). This method requires solving the fluid equations, for each species in the plasma, self-consistently, with Maxwell's equations; the fluid and EM equations are coupled through their source terms. To date, the algorithm has been demonstrated to solve the fluid equations only, handling regions of high energy (temperature) and strong spatial gradients - conditions often found in plasmas.

The current work extends the existing algorithm, applying similar discretization and numerical-stabilizing methods to solve the electromagnetic equations. This paper begins with a description of the governing

*Ph.D. Student, Member AIAA

†Associate Professor, Email: xinfeng.gao@colostate.edu, Member AIAA

equations, and then we discuss details of the numerical model. Next, accuracy of the method will be verified, and we will provide some validation examples for various test problems. Finally, we will discuss conclusions and future work.

III. Governing Equations

As the name suggests, the multi-fluid plasma model solves for the transport and evolution of each particle species separately (though coupled). When more than one species exist in the model, source terms for the electromagnetic equations become an amalgamation of multiple charge and current density values from all species in the domain. However, for the sake of simplicity, we focus here on the classical treatment of Maxwell's equations, where the charge and current densities at any point in the domain are represented by single terms. In other words, we consider a single species in this present work: electrons.

III.A. Classical form

A classical representation of Maxwell's equations is as follows:

$$\epsilon_0\mu_0\frac{\partial\vec{E}}{\partial t} = \vec{\nabla}\times\vec{B} - \mu_0\vec{j}, \tag{1}$$

$$\vec{\nabla}\cdot\vec{B} = 0, \tag{2}$$

$$\frac{\partial\vec{B}}{\partial t} = -\vec{\nabla}\times\vec{E}, \tag{3}$$

$$\vec{\nabla}\cdot\vec{E} = \frac{1}{\epsilon_0}\rho, \tag{4}$$

where $\vec{B}$ is the magnetic field, $\vec{E}$ is the electric field, $\vec{j}$ is the electric current density, and ρ is the electric charge density.

III.B. Hyperbolic-only formulation

The divergence relations imposed by Eq. (4) and Eq. (2) over-constrain the problem and can result in numerical error or instability. There are multiple approaches to handling this over-constraint. The method used in the current work involves introducing divergence correction potentials to form purely hyperbolic equations,[2–7] which take the following form

$$\epsilon_0\mu_0\frac{\partial\vec{E}}{\partial t} - \vec{\nabla}\times\vec{B} + \chi\nabla\Phi = -\mu_0\vec{j}, \tag{5}$$

$$\frac{\epsilon_0\mu_0}{\lambda}\frac{\partial\Psi}{\partial t} + \vec{\nabla}\cdot\vec{B} = 0, \tag{6}$$

$$\frac{\partial\vec{B}}{\partial t} + \vec{\nabla}\times\vec{E} + \lambda\nabla\Psi = 0, \tag{7}$$

$$\frac{1}{\chi}\frac{\partial\Phi}{\partial t} + \vec{\nabla}\cdot\vec{E} = \frac{1}{\epsilon_0}\rho. \tag{8}$$

Ψ and Φ are included as correction potentials, used to absorb any divergence errors. The dimensionless, positive, constants λ and χ determine the speed at which the divergence errors propagate out of the problem domain; they are scalar multipliers on the wave speed of the electromagnetic wave propagation (i.e. the speed of light, $c = 1/\sqrt{\epsilon_0\mu_0}$). These constants are set to values slightly greater than one in order to convect error out of the domain faster than the information wave speed without significantly increasing numerical stiffness.[2,5,7]

III.C. Normalized equations

The magnetic field $\vec{B}$ and electric field $\vec{E}$ are related through the electromagnetic properties of permittivity ($\epsilon_0 = 8.85 \times 10^{-12}$ F/m) and permeability ($\mu_0 = 1.26 \times 10^{-6}$ H/m. Because these are very small numbers, the quantities of $\vec{B}$ and $\vec{E}$ can differ by many orders of magnitude. To mitigate the risk of numerical overflow/underflow, we follow a similar approach to Yan and Jin,[7] electing to normalize the governing equations by the speed of light, $c = 1/\sqrt{\epsilon_0 \mu_0}$. The normalized (and simplified) quantities are as follows, where the original variable is denoted with superscript "o":

$$\vec{E} = \vec{E}^o \qquad \vec{B} = c\vec{B}^o \qquad \rho = \frac{\rho^o}{\epsilon_0} \qquad \vec{j} = \mu_0 \; c \; \vec{j}^o \tag{9}$$

Now, the purely-hyperbolic, electromagnetic equations can be re-written in terms of the normalized quantities. For the remainder of this paper, we refer to these normalized quantities and equations.

$$\frac{\partial \vec{E}}{\partial t} - c\vec{\nabla} \times \vec{B} + c\chi \nabla \Phi = -c\vec{j}, \tag{10}$$

$$\frac{\partial \Psi}{\partial t} + c\lambda \vec{\nabla} \cdot \vec{B} = 0, \tag{11}$$

$$\frac{\partial \vec{B}}{\partial t} + c\vec{\nabla} \times \vec{E} + c\lambda \nabla \Psi = 0, \tag{12}$$

$$\frac{\partial \Phi}{\partial t} + c\chi \vec{\nabla} \cdot \vec{E} = c\chi \rho. \tag{13}$$

III.D. Conservative form

For the convenience of algorithm implementation, the aforementioned electromagnetic equations — Eqs. (10) – (13) — can be written in conservative form, arranged in the following convention:

$$\frac{\partial \mathbf{U}}{\partial t} + \vec{\nabla} \cdot \vec{\mathbf{F}} = \mathbf{S}. \tag{14}$$

$\mathbf{U}$ is the vector of solution variables, $\vec{\mathbf{F}}$ is a dyadic tensor of hyperbolic flux terms, and $\mathbf{S}$ is a vector of source terms. In three-dimensional Cartesian coordinates, using the hyperbolic-only formation of Maxwell's equations, the solution vector $\mathbf{U}$ is arranged as follows:

$$\mathbf{U} = \left[E_x, E_y, E_z, \Psi, B_x, B_y, B_z, \Phi\right]^T. \tag{15}$$

The flux dyad in 3D, based on the normalized equations described in Section III.C is

$$\vec{\mathbf{F}} = \left[\begin{bmatrix} c\chi\Phi \\ cB_z \\ -cB_y \\ c\lambda B_x \\ c\lambda\Psi \\ -cE_z \\ cE_y \\ c\chi E_x \end{bmatrix}, \begin{bmatrix} -cB_z \\ c\chi\Phi \\ cB_x \\ c\lambda B_y \\ cE_z \\ c\lambda\,\Psi \\ -cE_x \\ c\chi\,E_y \end{bmatrix}, \begin{bmatrix} cB_y \\ -cB_x \\ c\chi\Phi \\ c\lambda B_z \\ -cE_y \\ cE_x \\ c\lambda\,\Psi \\ c\chi\,E_z \end{bmatrix} \right], \tag{16}$$

and the source vector takes on the following form:

$$\mathbf{S} = \left[-cj_x, -cj_y, -cj_z, 0, 0, 0, 0, c\chi\rho\right]^T . \tag{17}$$

As described earlier, when the electromagnetic equations are fully integrated into the multi-fluid plasma model, the charge and current density terms in the source vector become summations of the values from each fluid species; for example

$$\mathbf{S} = \left[-c\sum_\alpha q_\alpha j_{\alpha_x}, -c\sum_\alpha q_\alpha j_{\alpha_y}, -c\sum_\alpha q_\alpha j_{\alpha_z}, 0, 0, 0, 0, c\chi\sum_\alpha q_\alpha n_\alpha\right]^T , \tag{18}$$

for each charged species, α, in the domain. In this case, j_α terms represent the number density flux of species α, and n_α is the number density.

IV. Numerical Method

The computational framework for the present work is Chord,[8–13] our in-house CFD code. Chord is a fourth-order accurate, highly-parallelizable, finite-volume method algorithm, featuring adaptive mesh refinement (AMR) based on the Chombo library. Chord is designed to achieve high-performance, accurate solutions to problems involving complex physics, multi-scale behavior, and discontinuities such as turbulence, shocks, combustion, or plasmas. Chord ensures freestream preservation and enforces stability constraints. Chord also utilizes the loop chaining concept for significant improvement in code performance on parallel machines.

IV.A. Finite volume method

Finite-volume methods are well-suited for problems with discontinuities; the spatial discretization satisfies a discrete form of the divergence theorem, providing for a conservation-preserving solution in time. The solution-stabilizing and conservation-preserving nature of the FVM has been shown to be an accurate and efficient tool for solving the electromagnetic field equations.[4–6,14,15] Furthermore, the high-order finite-volume method has the ability to produce solutions for non-discontinuous problems much faster than low-order schemes, to the same level of accuracy. Also, high-order methods increase computation per unit memory, allowing for better use of current computer architectures.

For a finite-volume method on Cartesian grids, cell centers are marked by the points $(i_0, ..., i_{D-1}) = \boldsymbol{i} \in \mathbb{Z}^D$ and the faces by $\boldsymbol{i} \pm \frac{1}{2}\boldsymbol{e}^d$, where $\mathbf{e}^d$ is a unit vector in direction d. We start by integrating Eq. 14 over a control volume, V:

$$\frac{\partial}{\partial t}\int_V \mathbf{U}\,\mathrm{d}V + \int_V \left(\vec{\nabla}\cdot\vec{\mathbf{F}} - \mathbf{S}\right)\mathrm{d}V = 0\,. \tag{19}$$

Applying Gauss's divergence theorem to Eq. 19 over the control volume of cell $\boldsymbol{i}$, results in the following, semi-discrete form,

$$\frac{\mathrm{d}\langle\mathbf{U}\rangle_{\boldsymbol{i}}}{\mathrm{d}t} = -\frac{1}{\Delta x_d}\sum_{d=0}^{D-1}\left(\langle\vec{\mathbf{F}}\rangle_{\boldsymbol{i}+\frac{1}{2}\boldsymbol{e}^d} - \langle\vec{\mathbf{F}}\rangle_{\boldsymbol{i}-\frac{1}{2}\boldsymbol{e}^d}\right) + \langle\mathbf{S}\rangle_{\boldsymbol{i}}. \tag{20}$$

Now we have a system of ordinary differential equations (ODEs), where the integrals from Eq. (19) are represented by averages, $\langle\cdot\rangle$. To solve the system of ODEs, the spatial terms on the right hand side are evaluated, then the ODEs are evolved in time using standard, 4th-order, Runge-Kutta time marching.

IV.B. Flux calculation

The order of accuracy for a FVM is dependent on the spatial discretization scheme used to compute fluxes on the bounding surfaces of the control volume. Chord uses a fourth-order, center-differencing method for reconstructing the face-averaged quantities and the face-averaged gradients and thus for hyperbolic and elliptic flux evaluation. The hyperbolic flux is then evaluated based on the upwind scheme by solving a Riemann problem at each cell face. A piecewise parabolic method (PPM) limiter, as modified by McCorquodale and

Colella,[16] is used in the present implementation of Chord. Additionally, a slope flattening algorithm and optional, artificial viscosity can be added to the solution procedure to handle cases with sharp discontinuities or in cases were only inertial (hyperbolic) physics are being solved. For more detail on the spatial discretization, interested readers are referred to previous publications on Chord .[8–13]

Due to the numerical quadrature, each control volume in a domain has a unique approximation of $\langle \mathbf{U} \rangle$ and thus distinct values of flux $\langle \vec{\mathbf{F}} \rangle$ on either side of each face. To resolve these discontinuities, a solution to the initial value problem – based on the electromagnetic fluxes – needs to be determined for each face. As a starting point, we consider a Harten–Lax–van Leer contact wave (HLLC) method to approximate a solution to the Riemann problem (initial value problem).[15,17,18] In an improvement to the HLL scheme, the HLLC method restores the full wave structure inside the Riemann fan by replacing the single averaged state of the HLL scheme with two approximate states, $\mathbf{U}_L^*$ and $\mathbf{U}_R^*$. These states are separated by a contact wave in the middle, which is assumed to have a constant speed. The solution on the $x/t = 0$ axis is written as:

$$\mathbf{U}(0,t) = \begin{cases} \mathbf{U}_L & \text{if } \lambda_L \geq 0, \\ \mathbf{U}_L^* & \text{if } \lambda_L \leq 0 \leq \lambda^*, \\ \mathbf{U}_R^* & \text{if } \lambda^* \leq 0 \leq \lambda_R, \\ \mathbf{U}_R & \text{if } \lambda_R \leq 0, \end{cases} \tag{21}$$

where λ_L is the minimum characteristic wave speed, λ_R is the maximum wave speed, and λ^* is the contact wave speed. Consequently, the corresponding fluxes within each control volume are:

$$\mathbf{F}(0,t) = \begin{cases} \mathbf{F}_L & \text{if } \lambda_L \geq 0, \\ \mathbf{F}_L^* & \text{if } \lambda_L \leq 0 \leq \lambda^*, \\ \mathbf{F}_R^* & \text{if } \lambda^* \leq 0 \leq \lambda_R, \\ \mathbf{F}_R & \text{if } \lambda_R \leq 0. \end{cases} \tag{22}$$

The wave speeds for the electromagnetic physics are determined by solving for the eigenvalues of the flux Jacobian, $\partial \mathbf{F}/\partial \mathbf{U}$, and are written as

$$\mathbf{\Lambda} = \left[-\lambda c, \lambda c, -\chi c, \chi c, -c, -c, c, c\right]^T, \tag{23}$$

In a homogeneous medium, one can assume continuity of every conserved electromagnetic variable across the cell interface (contact wave). As previous authors have noted, the assumption of interfacial continuity for all conserved variables results in the HLLC fluxes reverting into the Godunov flux equations.[7,18] This is the approach we have used in the current work because it suffices for the simple, single-medium test cases considered in this paper. However, the full, HLLC Riemann solver algorithm is retained for future work involving domain discontinuities and heterogeneous medium.

IV.C. Boundary conditions

Boundary conditions are required to properly define the numerical domain. A well-posed boundary condition approach takes into account the direction of wave propagation and the theory of characteristics. Our approach involves prescribing artificial or ghost states outside the domain boundary and using the Riemann solver to resolve the discontinuity between the interiorly-interpolated state and the exteriorly-prescribed state. Two commonly used boundary conditions for the electromagnetic equations are examined, remembering that our notation at this point involves the normalized electromagnetic quantities and equations.

IV.C.1. Perfect electric conducting (PEC)

On a surface with perfect electrical conduction, there are no transverse electric fields, and thus, the normal component of the magnetic field is also zero. Furthermore, because we desire the divergence cleaning potentials to propagate error out of the domain, the boundary conditions for these values need to be prescribed accordingly. A Neumann type boundary condition is utilized for the scalar potential Ψ because a Dirichlet boundary is incompatible with the characteristic theory.[5] Written numerically, the definition of a PEC

boundary is

$$\vec{n} \times \vec{E^*} = 0, \tag{24}$$

$$\frac{\partial \Psi^*}{\partial n} = 0, \tag{25}$$

$$\vec{n} \cdot \vec{B^*} = 0, \tag{26}$$

$$\Phi^* = 0, \tag{27}$$

where the terms $\vec{U^*}$ and U^* refer to the state on the boundary face and $\vec{n}$ is the outward normal unit vector at the face. Accordingly, the exterior ghost states for the PEC boundary on a Cartesian mesh are

$$\begin{bmatrix} E_x^+ \\ E_y^+ \\ E_z^+ \\ \Psi^+ \\ B_x^+ \\ B_y^+ \\ B_z^+ \\ \Phi^+ \end{bmatrix} = \begin{bmatrix} E_x^- \\ -E_y^- \\ -E_z^- \\ \Psi^- \\ -B_x^- \\ B_y^- \\ B_z^- \\ -\Phi^- \end{bmatrix} \tag{28}$$

where the superscripts $+$ and $-$ refer to the faces outside and inside the domain, respectively.[5,7]

IV.C.2. Silver-Müller absorbing boundary condition (ABC)

To artificially truncate the domain without reflecting parasitic information to the interior, a Silver -Müller absorbing boundary condition is employed.

$$\left(\vec{E^*} - \vec{B^*} \times \vec{n}\right) \times \vec{n} = \left(\vec{E^{inc}} - \vec{B^{inc}} \times \vec{n}\right) \times \vec{n}, \tag{29}$$

$$\frac{\partial \Psi^*}{\partial n} = 0, \tag{30}$$

$$\Phi^* = 0, \tag{31}$$

where $\vec{E^{inc}}$ and $\vec{B^{inc}}$ are given fields along the boundary. The computation method of the ABC boundary is the same as the PEC boundary, but with different prescribed, exterior ghost states

$$\begin{bmatrix} E_x^+ \\ E_y^+ \\ E_z^+ \\ \Psi^+ \\ B_x^+ \\ B_y^+ \\ B_z^+ \\ \Phi^+ \end{bmatrix} = \begin{bmatrix} E_x^{inc} \\ E_y^{inc} \\ E_z^{inc} \\ -\Psi^- + \left(\vec{B^{inc}} - \vec{B^-}\right) \cdot \vec{n} \\ B_x^{inc} \\ B_y^{inc} \\ B_z^{inc} \\ -\Phi^- + \left(\vec{E^{inc}} - \vec{E^-}\right) \cdot \vec{n} \end{bmatrix}. \tag{32}$$

IV.D. AMR

AMR adjusts the mesh-resolution in response to the solution, increasing resolution in regions where the solution characteristics are discontinuous or feature strong gradients, and coarsening the mesh in quiescent regions to improve computational efficiency. Chord handles complex geometry by mapping structured grids in physical space to Cartesian grids in computational space. Cartesian grids are efficient, logistically simple, facilitate the use of AMR, and have well-understood solution accuracy properties. Interested readers are referred to previous publications on the implementation of AMR in Chord .[10,19]

V. Numerical Results

To verify the accuracy of our algorithm, and to validate the code against previous literature, we chose test cases with exact, analytical solutions. A three-dimensional, plane-polarized wave case is used to examine the stability and order of accuracy of our algorithm, and a transverse magnetic (TM) wave problem is used to assess the robustness of our implementation of a PEC boundary condition.

V.A. Three dimensional plane-polarized electromagnetic wave in vacuum

In this problem, a plane-polarized electromagnetic wave propagates across a three dimensional, vacuum domain with Cartesian coordinates $[0.0\,\text{m}, 1.0\,\text{m}]$ in each direction as illustrated in Figure 1. Periodic boundary conditions are used so the accuracy of the 4th-order interior scheme can be verified. The exact, electric and magnetic fields are given by the following equations:[20]

$$\vec{E}\,(x,y,z,t) = cos\left[2\pi\left(x+y+z-c\sqrt{3}\;t\right)\right]\left(0\hat{x} - \frac{1}{\sqrt{2}}\hat{y} + \frac{1}{\sqrt{2}}\hat{z}\right) \tag{33}$$

$$\vec{B}\,(x,y,z,t) = cos\left[2\pi\left(x+y+z-c\sqrt{3}\;t\right)\right]\left(\sqrt{\frac{2}{3}}\hat{x} - \frac{1}{\sqrt{6}}\hat{y} - \frac{1}{\sqrt{6}}\hat{z}\right) \tag{34}$$

where $\hat{x}$, $\hat{y}$, and $\hat{z}$ are the components of the $\vec{E}$ and $\vec{B}$ vectors in directions x, y, z. The test case was run over a range of mesh sizes, all to a final time of 1.2 ns. At the end of each simulation, the numerical solution was compared to the exact solution. The corresponding errors are evaluated using L_1, L_2, and L_∞ norms. Figure 2 shows the rate of error reduction with increasing mesh size; clearly, the slopes converge towards -4.0, verifying the fourth-order algorithm. Further, Table 1 lists the data for Figure 2, including the sequence of grids used, the error norms for both electric and magnetic field components, and error reduction rates between two consecutive mesh sizes.

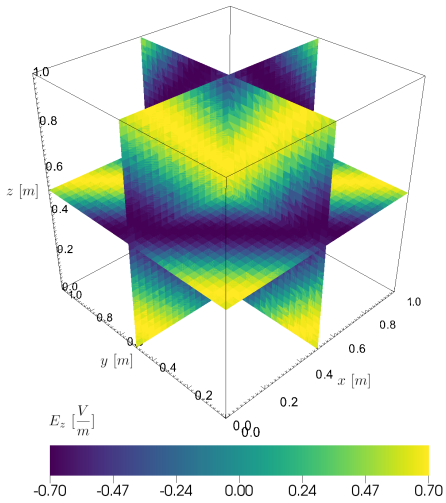

Figure 1: Three plane contour plot of variable E_z from the 3D electromagnetic wave test case, at time 1.2 ns.

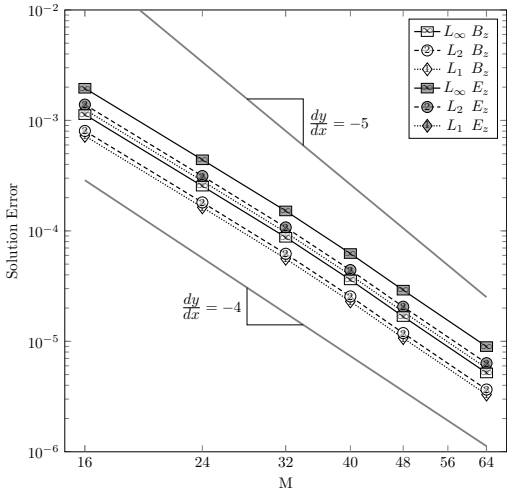

Figure 2: Grid convergence rate for variables E_z and B_z from the electromagnetic wave test case, at time 1.2 ns.

Table 1: Numerical values of the electromagnetic solution errors for the 3D plane-polarized electromagnetic wave test case at time 1.2 ns. The computed convergence rates are computed between consecutive grid resolutions, demonstrating the 4th-order accuracy of the algorithm.

	L **norm**	16^3	**rate**	24^3	**rate**	32^3	**rate**	40^3	**rate**	48^3	**rate**	64^3
E_y	L_1	1.25E-03	-3.67	2.83E-04	-3.73	9.69E-05	-3.99	3.98E-05	-4.19	1.85E-05	-4.09	5.71E-06
	L_2	1.39E-03	-3.67	3.14E-04	-3.72	1.07E-04	-3.98	4.42E-05	-4.19	2.06E-05	-4.09	6.34E-06
	L_∞	1.96E-03	-3.68	4.40E-04	-3.71	1.52E-04	-3.98	6.24E-05	-4.19	2.91E-05	-4.09	8.96E-06
E_z	L_1	1.25E-03	-3.67	2.83E-04	-3.73	9.69E-05	-3.99	3.98E-05	-4.19	1.85E-05	-4.09	5.71E-06
	L_2	1.39E-03	-3.67	3.14E-04	-3.72	1.07E-04	-3.98	4.42E-05	-4.19	2.06E-05	-4.09	6.34E-06
	L_∞	1.96E-03	-3.68	4.40E-04	-3.71	1.52E-04	-3.98	6.24E-05	-4.19	2.91E-05	-4.09	8.96E-06
B_x	L_1	1.45E-03	-3.67	3.27E-04	-3.73	1.12E-04	-3.99	4.60E-05	-4.19	2.14E-05	-4.09	6.60E-06
	L_2	1.60E-03	-3.67	3.62E-04	-3.72	1.24E-04	-3.98	5.10E-05	-4.19	2.37E-05	-4.09	7.32E-06
	L_∞	2.26E-03	-3.68	5.08E-04	-3.71	1.75E-04	-3.98	7.20E-05	-4.19	3.35E-05	-4.09	1.04E-05
B_y	L_1	7.24E-04	-3.67	1.63E-04	-3.73	5.59E-05	-3.99	2.30E-05	-4.19	1.07E-05	-4.09	3.30E-06
	L_2	8.02E-04	-3.67	1.81E-04	-3.72	6.21E-05	-3.98	2.55E-05	-4.19	1.19E-05	-4.09	3.66E-06
	L_∞	1.13E-03	-3.68	2.54E-04	-3.71	8.75E-05	-3.98	3.60E-05	-4.19	1.68E-05	-4.09	5.18E-06
B_z	L_1	7.24E-04	-3.67	1.63E-04	-3.73	5.59E-05	-3.99	2.30E-05	-4.19	1.07E-05	-4.09	3.30E-06
	L_2	8.02E-04	-3.67	1.81E-04	-3.72	6.21E-05	-3.98	2.55E-05	-4.19	1.19E-05	-4.09	3.66E-06
	L_∞	1.13E-03	-3.68	2.54E-04	-3.71	8.75E-05	-3.98	3.60E-05	-4.19	1.68E-05	-4.09	5.18E-06

V.B. Transverse magnetic wave

Another class of electromagnetic test cases with exact solutions are the various waveguide modes: transverse magnetic (TM), transverse electric (TE), and transverse electromagnetic (TEM). In particular, a TM wave simulation considered in previous literature[5] provides a relevant validation test for our current work. In this test case, a rectangular, two-dimensional plane represents a cross-section of a waveguide. The domain size is $L_x = 80\,\text{m}$ and $L_y = 40\,\text{m}$. The wavenumbers are given by

$$a = \frac{m\pi}{L_x} \qquad\qquad b = \frac{n\pi}{L_y}, \tag{35}$$

where $m = 8$, $n = 5$. The net wave travels in the z direction, oscillating at the cutoff frequency, ω. The exact solution for this problem is given by equations Eqs. (36) – (38),

$$E_z = \Re(E_0 \sin(ax) \sin(by) e^{-j\omega t}), \tag{36}$$

$$B_x = \Re(-j\frac{b}{\omega} E_0 \sin(ax) \cos(by) e^{-j\omega t}), \tag{37}$$

$$B_y = \Re(j\frac{a}{\omega} E_0 \cos(ax) \sin(by) e^{-j\omega t}), \tag{38}$$

where $\Re$ denotes the real component of the complex expressions, j is the imaginary unit, and E_0 is the initial electric field value ($1\,\text{V/m}$ in our test case).

The TM wave problem is modeled with PEC boundary conditions and initialized using the analytical solution data at time $t = 0$. The divergence cleaning potentials are both initialized to zero. The wave speed scalars used on the divergence cleaning potentials Ψ and Φ are $\lambda = 1.0$ and $\chi = 0.0$, respectively. The solution is advanced in time using a CFL number of 0.8.

The scalar electric field, E_z oscillates in time according to the analytical solution and numerical damping of the magnitude is minimized by the 4th-order algorithm as shown in Figure 3. Line samples of the simulation results at 75 ns compare well with the exact solution, as shown in Figure 4, and are also consistent with higher-order, numerical methods used in previous literature.[5] As the solution advances in time, the initial electric field gradients drive the evolution of rotating magnetic fields (Figure 5). The shape and magnitudes of the magnetic fields are symmetric and also appear to free from adverse affects from the physical boundary.

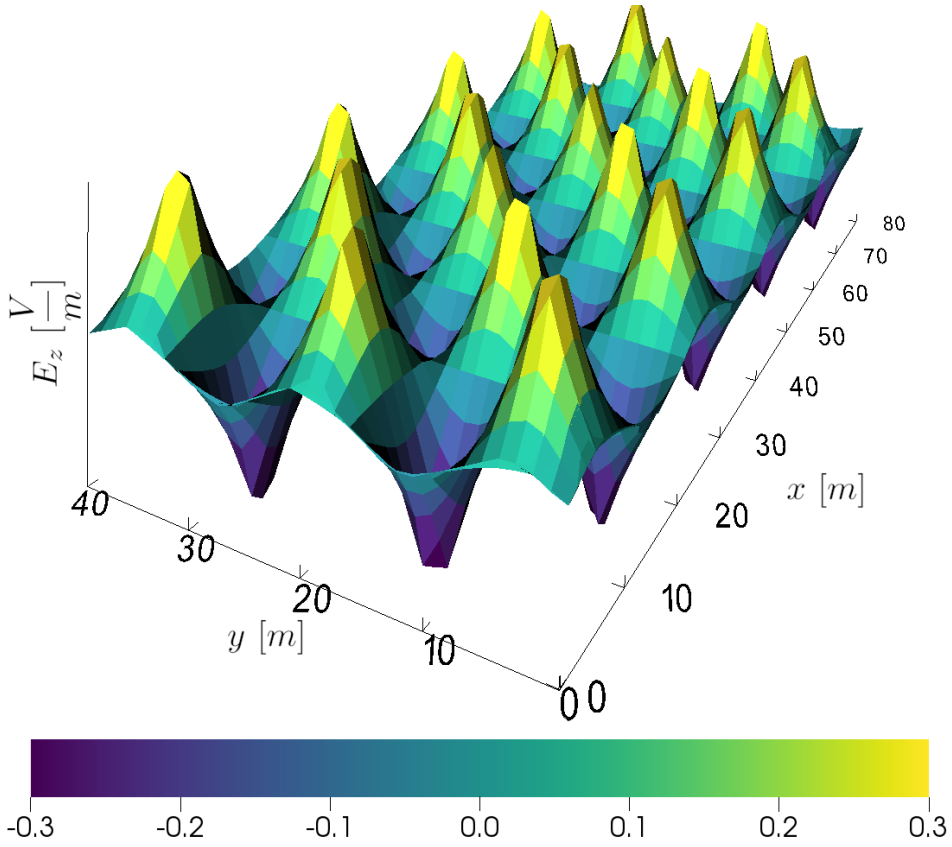

Figure 3: Transverse magnetic wave solution for scalar electric field E_z with $m = 8$ and $n = 5$, at solution time 75 ns on a 64×32 mesh.

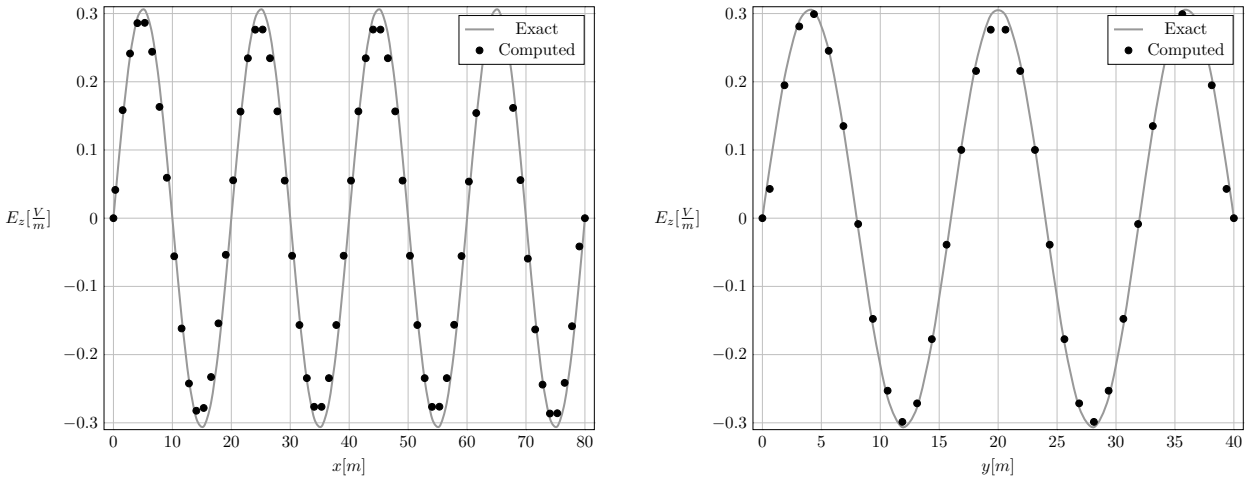

Figure 4: Comparison of numerical results for the TM wave calculation on a 64×32 mesh, with $m = 8$ and $n = 5$, at solution time 75 ns. Left plot shows E_z at $y = 20[m]$ and right plot shows E_z at $x = 25[m]$. The numerical results (black marks) show good agreement with the exact solution (solid lines).

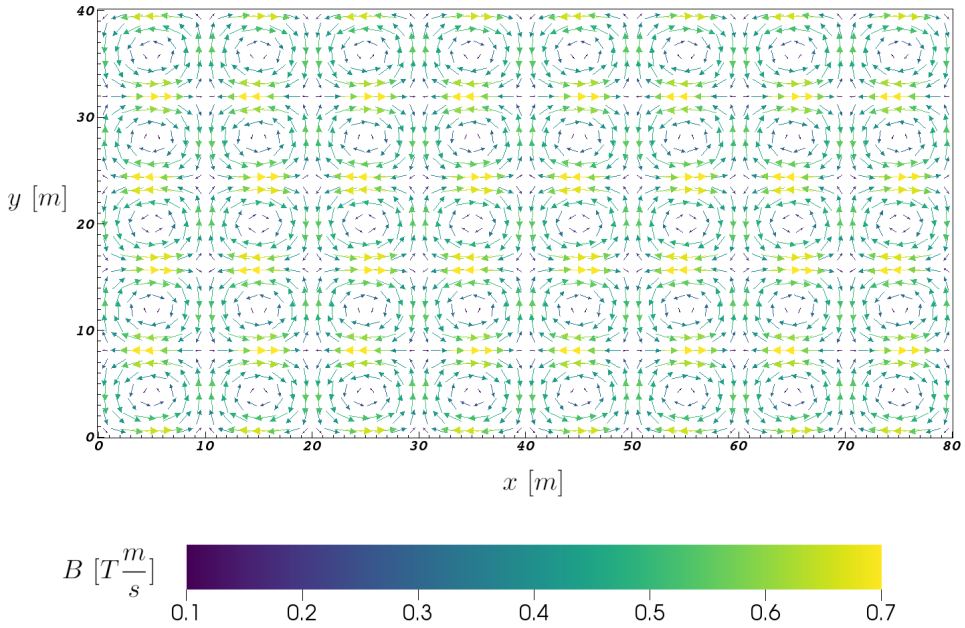

Figure 5: Transverse magnetic wave solution for magnetic field $\vec{B}$ with $m = 8$ and $n = 5$, at solution time 75 ns on a 64×32 mesh.

VI. Concluding Remarks and Future Work

In the present work, we have constructed a three-dimensional, finite-volume solver for the equations of electromagnetic wave propagation. We utilize the technique of including additional degrees of freedom in the electromagnetic equations to account for errors in the divergence terms, which also allows for the differential equations to be represented in a purely hyperbolic form. The algorithm is 4th-order accurate in both space and time. We leverage the PPM limiter during reconstruction of the cell face values.[16] An HLLC-type Riemann solver is used to resolve the discontinuities at the cell faces, including boundary faces, and compute the flux. A simplification of the HLLC solver can be preformed if one assumes continuity of all conserved variables across the cell interface - an assumption we have made initially, to facilitate verification of our algorithm.

We have verified fourth-order accuracy and validated the code against a plane-polarized, three-dimensional wave propagation problem as well as a transverse magnetic wave problem, both of which have exact solutions. Both test cases involve homogeneous vacuum domains with either PEC or periodic type boundary conditions.

Our next steps will include further exploration of the use and effects of divergence cleaning potentials on solution accuracy and computational efficiency. Additionally, we are working on including the capability for problems with heterogeneous media. AMR will be particularly well suited to handle the gradients and discontinuities which are expected to form at interfaces between cells with disparate electromagnetic properties. Furthermore, we seek to improve the accuracy of the existing boundary conditions, as well as implement other, common, electromagnetic boundary types.

Long-term, we plan on implementing grid mapping to handle non-Cartesian meshes and geometry. Ultimately, we will couple the electromagnetic solver into the previously-discussed, multi-fluid plasma code we are developing.[1]

References

[1]Polak, S. and Gao, X., "A Fourth-Order Finite-Volume Method with Adaptive Mesh Refinement for the Multifluid Plasma Model," *2018 AIAA Aerospace Sciences Meeting, AIAA SciTech Forum, American Institute of Aeronautics and Astronautics*, 2018.

[2]Sousa, E. and Shumlak, U., "A blended continuous-discontinuous finite element method for solving the multi-fluid plasma model," *Journal of Computational Physics*, Vol. 326, Dec. 2016, pp. 56–75.

[3]Shumlak, U., Lilly, R., Reddell, N., Sousa, E., and Srinivasan, B., "Advanced physics calculations using a multi-fluid plasma model," *Computer Physics Communications*, Vol. 182, No. 9, Sept. 2011, pp. 1767–1770.

[4]Munz, C.-D., Omnes, P., and Schneider, R., "A Godunov-type Solver for the Maxwell Equations with Divergence Cleaning," *Godunov Methods*, edited by E. F. Toro, Springer US, 2001, pp. 647–654, DOI: 10.1007/978-1-4615-0663-8_64.

[5]Munz, C.-D., Ommes, P., and Schneider, R., "A three-dimensional finite-volume solver for the Maxwell equations with divergence cleaning on unstructured meshes," *Computer Physics Communications*, Vol. 130, No. 1-2, July 2000, pp. 83–117.

[6]Munz, C.-D., Omnes, P., Schneider, R., Sonnendrücker, E., and Voß, U., "Divergence Correction Techniques for Maxwell Solvers Based on a Hyperbolic Model," *Journal of Computational Physics*, Vol. 161, No. 2, July 2000, pp. 484–511.

[7]Yan, S. and Jin, J.-M., "A continuity-preserving and divergence-cleaning algorithm based on purely and damped hyperbolic Maxwell equations in inhomogeneous media," *Journal of Computational Physics*, Vol. 334, apr 2017, pp. 392–418.

[8]Gao, X., Guzik, S. M. J., and Colella, P., "Fourth Order Boundary Treatment for Viscous Fluxes on Cartesian Grid Finite-Volume Methods," AIAA 2014-1277, 52nd AIAA Aerospace Sciences Meeting, 2014.

[9]Gao, X. and Guzik, S. M. J., "A Fourth-Order Scheme for the Compressible Navier-Stokes Equations," AIAA 2015-0298, 53rd AIAA Aerospace Sciences Meeting, 2015.

[10]Guzik, S. M., Gao, X., Owen, L. D., McCorquodale, P., and Colella, P., "A Freestream-Preserving Fourth-Order Finite-Volume Method in Mapped Coordinates with Adaptive-Mesh Refinement," *Comput. Fluids*, Vol. 123, 2015, pp. 202–217.

[11]Guzik, S. M., Gao, X., and Olschanowsky, C., "A high-performance finite-volume algorithm for solving partial differential equations governing compressible viscous flows on structured grids," *Comput. Math Appl.*, Vol. 72, 2016, pp. 2098–2118.

[12]Gao, X., Owen, L. D., and Guzik, S. M. J., "A Parallel Adaptive Numerical Method with Generalized Curvilinear Coordinate Transformation for Compressible Navier-Stokes Equations," *Int. J. Numer. Meth. Fluids*, Vol. 82, 2016, pp. 664–688.

[13]Gao, X., Owen, L. D., and Guzik, S. M., "A High-Order Finite-Volume Method for Combustion," AIAA 2016-1808, 54th AIAA Aerospace Sciences Meeting, 2016.

[14]Yee, K. S. and Chen, J. S., "The finite-difference time-domain (FDTD) and the finite-volume time-domain (FVTD) methods in solving Maxwell's equations," *IEEE Transactions on Antennas and Propagation*, Vol. 45, No. 3, Mar 1997, pp. 354–363.

[15]Mignone, A. and Bodo, G., "An HLLC Riemann solver for relativistic flows - II. Magnetohydrodynamics," *Monthly Notices of the Royal Astronomical Society*, Vol. 368, No. 3, 2006, pp. 1040–1054.

[16]McCorquodale, P. and Colella, P., "A high-order finite-volume method for conservation laws on locally refined grids," *Comm. App. Math. Comput. Sci.*, Vol. 6, No. 1, 2011, pp. 1–25.

[17]Mignone, A. and Bodo, G., "An HLLC Riemann solver for relativistic flows - I. Hydrodynamics," *Monthly Notices of the Royal Astronomical Society*, Vol. 364, No. 1, 2005, pp. 126–136.

[18]Miranda-Aranguren, S., Aloy, M. A., and Rembiasz, T., "An HLLC Riemann solver for resistive relativistic magnetohydrodynamics," *Monthly Notices of the Royal Astronomical Society*, Vol. 476, No. 3, feb 2018, pp. 3837–3860.

[19]Berger, M. J. and Colella, P., "Local Adaptive Mesh Refinement for Shock Hydrodynamics," *J. Comput. Phys.*, Vol. 82, No. 1, May 1989, pp. 64–84.

[20]Balsara, D. S., Amano, T., Garain, S., and Kim, J., "A high-order relativistic two-fluid electrodynamic scheme with consistent reconstruction of electromagnetic fields and a multidimensional Riemann solver for electromagnetism," *Journal of Computational Physics*, Vol. 318, aug 2016, pp. 169–200.